

Integral Line-of-Sight Path Following Control of Magnetic Helical Microswimmers Subject to Step-Out Frequencies

Alireza Mohammadi ^a, Mark W. Spong ^b

^a*Department of Electrical & Computer Engineering, University of Michigan, Dearborn*

^b*Erik Jonsson School of Engineering & Computer Science, University of Texas, Dallas*

Abstract

This paper investigates the problem of straight-line path following for magnetic helical microswimmers. The control objective is to make the helical microswimmer to converge to a straight line without violating the step-out frequency constraint. The proposed feedback control solution is based on an optimal decision strategy (ODS) that is cast as a trust-region subproblem (TRS), i.e., a quadratic program over a sphere. The ODS-based control strategy minimizes the difference between the microrobot velocity and an integral line-of-sight (ILOS)-based reference vector field while respecting the magnetic saturation constraints and ensuring the absolute continuity of the control input. Due to the embedded integral action in the reference vector field, the microswimmer will follow the desired straight line by compensating for the drift effect of the environmental disturbances as well as the microswimmer weight.

Key words: Magnetic microswimmers; control input saturation; path following control; integral line-of-sight guidance law.

1 Introduction

Swimming microrobots can be used for both *in vivo* and *in vitro* biomedical and micromanipulation applications. In *in vivo* biomedical applications, these robotic microswimmers can be employed for minimally invasive therapeutic and diagnostic procedures [1, 2]. In *in vitro* or lab-on-a-chip applications, these robots can be used for protein-crystal handling [3] and cell manipulation/characterization [4]. Microrobots can be categorized based on their morphologies and actuators [5]. Among the two main classes of actuation methods for microswimmers, i.e., *untethered magnetic actuation* [5, 6] and *molecular motors* [7], using external magnetic fields for control of untethered microswimmers is more popular; mainly because the former scales well in terms of microfabrication and wireless power transmission/control.

The type of the microswimmer morphology is another factor that should be taken into account for microrobot

design. Bead-like [8], eukaryotic-like [7, 9], and helical [10, 11] shapes are the most widely-used morphologies for magnetic microswimmers. Magnetic microbeads are tiny rigid objects that are pulled through fluids using magnetic field gradients [5]. In contrast to employing helical propellers or elastic tails, using magnetic gradient pulling is far less efficient in terms of propulsion efficiency due to limitations on magnetic field sources. As shown by [5], there exists a microrobot size below which employing helical propellers and elastic tails is more efficient than pulling microbeads with field gradients. Robotic microswimmers with eukaryotic-like morphologies move in their fluid environments by oscillating their flexible elastic tails. On the other hand, in helical microswimmers, propulsive forces on the nanocoil structure are generated due to the rotation of the microrobot about the axis of its helix. Although the main mechanism for both elastic-tail and helical-propeller magnetic microswimmers is based on transduction of magnetic torque to mechanical power, the helical morphology, which is inspired by bacterial flagella, has been shown to provide the best overall choice for *in vivo* applications [5]. Ease of direction reversal, independence of the microswimmer functionalization (e.g., drug coating) from fluid-dynamic properties, smooth transition from lumen to open environments, and the possibility of us-

* This paper was not presented at any IFAC meeting. Corresponding author A. Mohammadi. Tel. +1-313-583-6787.

Email addresses: amohammad@umich.edu (Alireza Mohammadi), mspong@utdallas.edu (Mark W. Spong).

ing non-uniform magnetic fields are among the principal reasons for superiority of helical propellers with respect to their elastic tail counterparts.

Along with recent advances in microfabrication and actuation technologies, systematic design of automatic motion control algorithms for magnetic microswimmers has also been an active area of research [11–16]. Being susceptible to gravity and body fluid drag force uncertainties, limited accuracy and low localization rates in small scales, and limitations on electromagnetic actuators are among the most significant challenges that arise in closed-loop control of magnetic microswimmers. The typical control approach in microrobot motion control literature relies on asymptotic tracking of suitably designed reference signals either in the form of a sequence of waypoints or in the form of time-based trajectories. Dahroug *et al.* [17] have recently shown via experiments that trajectory tracking control strategies are not robust to time delays and may create geometric deviations from the desired paths in low Reynolds swimming. Indeed, as demonstrated by Aguiar *et al.* [18], trajectory tracking controllers for even LTI systems are subject to performance limitations in the presence of structural system constraints such as nonminimum phase zeros.

Few researchers have proposed path following controllers for magnetic microswimmers [19–22]. The core of the underlying idea in [19–22] relies on proper state transformations using the geometry of the target curved path in order to bring the dynamics of the microrobots into a chained form. Then, nonholonomic control techniques inspired by Samson and collaborators (see, e.g., [23]) are invoked in order to make the microrobot to converge to the target path with a desired velocity profile. In [20], the authors generalized the approach in [19] from planar path following to 3D path following by devising non-holonomic control laws for higher dimension chained dynamics. In [22], the Serret–Frenet frame considering the weight of the robot and lateral disturbances using the compensation inclination and direction angles has been employed. In [21], orientation-compensation model of the microrobot dynamics in the global coordinate frame is learned by proper backpropagation algorithms. However, the proposed path following schemes do not directly address the control input saturation and the presence of unknown disturbances for the full dynamical model of the microswimmers.

Magnetic microbead control is perhaps the most researched topic in the area of magnetic microswimmer control where a plethora of control schemes ranging from simple PID to adaptive backstepping controllers have been proposed in the literature. Marino *et al.* [12] have employed robust \mathcal{H}_∞ synthesis techniques to address steering of magnetic microbeads in motionless fluids under drag-force uncertainties and low image acquisition rates. Fruchard *et al.* [13] propose using an adaptive backstepping control law along with a high gain observer for estimating the microbead velocity (see, also, [13]).

Unlike magnetic microbeads, very few control solutions for eukaryotic-like microswimmers have been proposed in the literature (see, e.g. [9, 24]). Many of these solutions rely on applying open-loop sinusoidal control inputs or designing linear controllers for Galerkin projection of the underlying elastic tail dynamical model. A recent promising approach to synthesis of propulsive gaits for microswimmers with elastic tails is based on small-compliance assumptions and applying asymptotic perturbation techniques to the equations of motion [25].

Early control solutions for magnetic helical microrobots have relied on considering the one-dimensional motion of the microswimmer along its helical axis [10, 19, 26, 27] without considering the effect of the microswimmer weight and/or other types of environmental disturbances. In a recent work, Mahoney *et al.* [11] use an open-loop gravity compensation method for velocity control of helical magnetic microrobots that sink due to their own weights. The control-oriented model developed by Mahoney *et al.* does not assume neutral buoyancy of artificial helical microswimmers while directly taking into account the sinking effect of the microswimmer weight.

In addition to the presence of disturbances, another major control challenge for magnetic helical microrobots is due to the existence of an upper limit on the robot rotational frequency around its helical axis. This threshold frequency, which is the maximum rotational frequency that keeps the robot in synchrony with the external rotating field, is known as the *step-out frequency* beyond which the velocity of the microswimmer rapidly declines [5, 28]. In addition to rotating in sync with the magnetic field, most researchers also assume alignment of the field rotation axis with the microswimmer helical axis (see, e.g., [11]).

In this paper, we present a path following control law that formally guarantees practical convergence of magnetic microswimmers to desired straight lines with absolutely continuous velocity profiles while respecting the control input saturation limits in the presence of disturbances. Our path following scheme uses an optimal decision strategy (ODS)-based control synthesis approach. ODS-based strategies belong to the larger family of optimization-based nonlinear controllers [29–31], whose applications in robotics and driverless cars are growing, thanks in part to recent advancements in mobile computation power. Optimal decision strategies, which were originally proposed in the context of controlling electric power systems and industrial robotic manipulators with bounded input [32–34], are *pointwise optimal control laws* that minimize the deviation between the open-loop dynamics vector field and a reference model vector field. We propose using an integral line-of-sight (ILOS)-based reference vector field for our ODS-based control scheme inspired from the ILOS path following laws that are widely used for underactuated marine craft control [35, 36]). Our proposed ILOS-based guid-

ance law incorporates the integral of the cross-track error of the microswimmer to the straight line.

Since our proposed ODS-based QP, which computes control actions using the ILOS-based guidance law, has constraints on the magnitude of the control input vector, it belongs to the family of trust-region subproblems (TRS), i.e., QPs over spheres and ellipsoids [37, 38]. TRS has long been of interest to the optimization research community (see, e.g., the classical work by Forsythe and Golub [39]); because a TRS needs to be solved in each step of trust-region optimization algorithms. In this paper, we provide the necessary and sufficient conditions for the existence of solutions to the special TRS that arises in the context of the magnetic microswimmer control problem. Furthermore, we provide sufficient conditions under which the absolute continuity of the generated control input is guaranteed. The absolute continuity of the control input is not only appealing from an existence and uniqueness of solutions perspective, but is also significant from a practical point of view. Indeed, it has been observed in practice that as long as a helical microswimmer is commanded a smooth desired-velocity profile with limits on acceleration, the *highly correlated* requirements of rotating below the step-out frequency as well as alignment of the field rotation axis with the microrobot axis will be met [11].

Contributions of the paper. This paper contributes to solving the path following control problem for swimming helical microrobots in *several ways*. First, the paper develops an ILOS-based guidance law for swimming microrobots, which is inspired from the automatic ship steering literature [35, 36, 40]. In the presence of disturbances that drive the microswimmer away from its desired path, embedding the integral compensation dynamics will build up a corrective action in the reference vector field. Second, using the ILOS-based guidance law, this paper casts the control input computation as a trust-region subproblem (TRS), i.e., a quadratic program over a sphere, which belongs to the wider class of real-time optimization-based controllers. In our previous work [15], we also used the ODS framework for designing path following controllers for magnetic helical microswimmers. While the proposed ODS-based controller in [15], which is based on the traditional line-of-sight (LOS) guidance law, respects the step-out frequencies, it relies on the full knowledge of the microswimmer dynamical parameters and assumes absence of disturbances. Additionally, the controller in [15] formally guarantees neither the continuity of the control inputs nor the continuity of the commanded desired-velocity profiles. In this paper, we relax many of our prior assumptions.

The rest of this paper is organized as follows. First, we present the dynamical model of swimming helical microrobots in Section 2. Next, we formulate the straight-line path following control problem for a single swimming microrobot subject to control input constraints and out-

line our solution strategy in Section 3. Thereafter, we present our ODS-based control scheme for swimming helical microrobots in Section 4. After presenting the simulation results in Section 5, we conclude the paper with final remarks and future research directions in Section 6.

Notation. We let \mathbb{R}_+ denote the set of all non-negative real numbers. Given a vector $\mathbf{v} \in \mathbb{R}^3$ and two coordinate frames \mathcal{A} and \mathcal{B} , we let ${}^{\mathcal{A}}\mathbf{v}$ and ${}^{\mathcal{B}}\mathbf{v}$ be the coordinates of \mathbf{v} in \mathcal{A} and \mathcal{B} , respectively. Therefore, ${}^{\mathcal{A}}\mathbf{v} = {}^{\mathcal{A}}\mathbf{R}_{\mathcal{B}}{}^{\mathcal{B}}\mathbf{v}$, where ${}^{\mathcal{A}}\mathbf{R}_{\mathcal{B}} \in \text{SO}(3)$ is the rotation matrix from the frame \mathcal{B} to the frame \mathcal{A} . Given $\mathbf{x} \in \mathbb{R}^N$, we let $\|\mathbf{x}\| := \sqrt{\mathbf{x}^\top \mathbf{x}}$ denote the Euclidean norm of \mathbf{x} . We let $\mathcal{B}_{r_0}(\mathbf{x}_0) := \{\mathbf{x} \in \mathbb{R}^N : \|\mathbf{x} - \mathbf{x}_0\| < r_0\}$ denote the ball centered at \mathbf{x}_0 with radius r_0 . Given two vectors \mathbf{v}_1 and \mathbf{v}_2 and a coordinate frame \mathcal{A} , the dot product of the two vectors is denoted by $\mathbf{v}_1 \cdot \mathbf{v}_2 := |\mathbf{v}_1| |\mathbf{v}_2| \cos(\theta)$, where θ is the angle between the two vectors \mathbf{v}_1 and \mathbf{v}_2 . Hence, $\mathbf{v}_1 \cdot \mathbf{v}_2 = {}^{\mathcal{A}}\mathbf{v}_1^\top {}^{\mathcal{A}}\mathbf{v}_2$. Given a square symmetric matrix \mathbf{A} , we let $\lambda_{\min}(\mathbf{A})$ and $\lambda_{\max}(\mathbf{A})$ denote the minimum and maximum eigenvalues of \mathbf{A} , respectively. Furthermore, we let $\mathbf{A} \succeq 0$ denote positive semi-definiteness of \mathbf{A} . We let $\mathbb{1} : \mathbb{R} \rightarrow \{0, 1\}$ denote the Heaviside step function, where $\mathbb{1}(x) = 1$ if $x \geq 0$, and $\mathbb{1}(x) = 0$ if $x < 0$. Given a piecewise continuous function $\mathbf{u} : \mathbb{R}_+ \rightarrow \mathbb{R}^m$, we let $\|\mathbf{u}\|_\infty := \sup_{t \in \mathbb{R}_+} \max_{1 \leq i \leq m} |u_i(t)|$.

2 Dynamical Model of Magnetic Helical Microswimmers

In this section we present the dynamics of magnetic helical microswimmers and summarize the results in [11].

We consider the line \mathcal{P} to which we would like the microswimmer to converge. We designate an arbitrary reference point $O_{\mathcal{W}}$ on \mathcal{P} as the origin. Assuming that \mathcal{P} is parallel to the direction vector $\hat{\mathbf{e}}_r \in \mathbb{R}^3$, we have

$$\mathcal{P} = \{\mathbf{p} \in \mathbb{R}^3 : \mathbf{p} = \tau \hat{\mathbf{e}}_r, \tau \in \mathbb{R}\}. \quad (1)$$

Considering the gravitational acceleration vector \mathbf{g} , we define $\hat{\mathbf{e}}_x$ to be the unit vector that is perpendicular to \mathbf{g} and is contained in the plane spanned by \mathcal{P} and \mathbf{g} . We fix the right-handed inertial coordinate frame \mathcal{W} at $O_{\mathcal{W}}$ using the unit vectors $\hat{\mathbf{e}}_x$, $\hat{\mathbf{e}}_z := \frac{-\mathbf{g}}{|\mathbf{g}|}$, and $\hat{\mathbf{e}}_y := \hat{\mathbf{e}}_x \times \hat{\mathbf{e}}_z$ (see Figure 1(a)).

Remark 2.1 *If the desired path \mathcal{P} is parallel to \mathbf{g} , we choose another arbitrary line \mathcal{P}' and fix the right-handed inertial coordinate frame \mathcal{W} using \mathbf{g} and \mathcal{P}' .*

In addition to the inertial coordinate frame \mathcal{W} , we also consider the coordinate frame \mathcal{H} , whose origin $O_{\mathcal{H}}$ is located at the helix center. We let the x-axis of \mathcal{H} , which we denote by $\mathbf{x}_{\mathcal{H}}$, be aligned with the microrobot helical axis. We let the z-axis of the frame \mathcal{H} be the axis

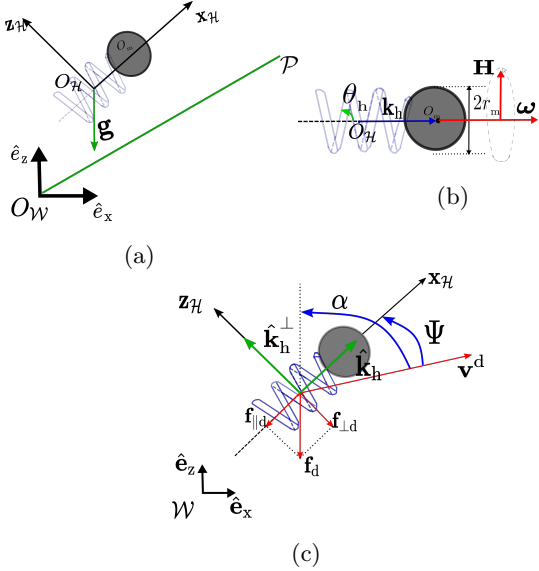


Fig. 1. The configuration of a magnetic helical microrobot.

\mathbf{z}_H that is perpendicular to \mathbf{x}_H and is contained in the plane spanned by \mathbf{x}_H and \mathbf{g} (see Figure 1(a)). The helical microswimmer geometry is completely determined by the number of turns of the helix n_h , the helix pitch angle θ_h , the helix coil thickness r_c , the helix radius r_h , and the magnetic head radius r_m (see Figure 1(b)). We let \mathbf{k}_h denote the vector connecting the center of the helix O_H to the center of the magnetic head O_m . Therefore, $\hat{\mathbf{k}}_h := \frac{\mathbf{k}_h}{|\mathbf{k}_h|}$ is parallel to the \mathbf{x}_H axis. In Figure 1(b), the magnetic field vector, which is induced by an external magnetic source, is shown by vector \mathbf{H} . The rotation of the field vector \mathbf{H} causes the magnetic helical micro-robot to rotate about its axis with an angular velocity vector given by $\boldsymbol{\omega}$ shown in Figure 1(b). Figures 1(a) and 1(b) depict the configuration of a generic helical microrobot as well as the coordinate frames \mathcal{W} and \mathcal{H} . In this paper, we consider the wireless magnetic swimming of microrobots with helical propellers in low-Reynolds-number regimes. The Reynolds (Re) number, which is used for studying propulsion mechanisms in fluidic environments, represents the ratio between the inertial forces and the resistive forces in a fluid. We denote the parallel and normal viscous drag force coefficients of the helical microswimmer by ξ_{\perp} and ξ_{\parallel} , respectively. Furthermore, we let ξ_{vm} denote the drag force coefficient of the microswimmer's spherical magnetic head.

The microrobot propulsion mechanism, which is based on transducing the external magnetic field energy to microrobot forward motion, can be described as follows. An external rotating uniform magnetic field, denoted by \mathbf{H} in Figure 1(b), causes the magnetic helical microrobot to rotate about its axis with an angular velocity vector given by $\boldsymbol{\omega}$. The resulting rotation about the helix in the ambient fluidic environment will then induce a screw-like motion and drive the microswimmer forward.

In this paper, we use the control-oriented model developed in [11]. Using resistive force theory (RFT), Mahoney *et al.* [11] have derived the dynamical model of 3D helical microswimmers operating in low-Reynolds-number regimes. In this approach, the velocity of each infinitesimally small helix segment is mapped to parallel and perpendicular differential fluid drag forces acting on the segment. Integrating the differential forces along the length of the helix, the fluidic force and torque acting on the helical part of the robot are obtained. Adding the fluidic forces acting on the head, the dynamical equations of motion are obtained. In deriving their control-oriented dynamical model and later experimental implementations, Mahoney *et al.* [11] assume the following.

H1) The helical magnetic microswimmer rotates in synchrony with the external magnetic field. This assumption implies that the commanded rotation speed $|\boldsymbol{\omega}|$ is not above the step-out frequency Ω_{SO} of the microswimmer, beyond which the velocity of the microswimmer rapidly declines [28].

H2) The central axis of the microswimmer \mathbf{x}_H is always aligned with the magnetic field rotation axis. In other words, the angular velocity of the microswimmer can be directly commanded to be

$$\boldsymbol{\omega} = \Omega \hat{\mathbf{k}}_h, \quad (2)$$

where Ω is the rotational frequency of the helical microswimmer about its axis.

Remark 2.2 *It is known from the experimental observations (see, e.g., [5, 11]) that as long as the microrobot is commanded a smooth velocity profile with limits on acceleration, the highly correlated requirements of rotating below the step-out frequency (required by H1) as well as alignment of the field rotation axis with the microrobot axis (required by H2) will be met in practice. As it will be shown in this paper, our control scheme formally guarantees that the commanded velocity respects both the step-out frequency constraint and the smoothness requirement.*

In the inertial coordinate system \mathcal{W} , the velocity of the microswimmer \mathbf{v} is related to applied non-fluidic forces \mathbf{f}_d and the angular velocity of the microswimmer $\boldsymbol{\omega}$, which represents the applied control input, through [11]

$${}^{\mathcal{W}}\mathbf{v} = {}^{\mathcal{W}}\mathbf{D}{}^{\mathcal{W}}\mathbf{f}_d + {}^{\mathcal{W}}\mathbf{E}{}^{\mathcal{W}}\boldsymbol{\omega}, \quad (3)$$

where the matrices ${}^{\mathcal{W}}\mathbf{D}, {}^{\mathcal{W}}\mathbf{E} \in \mathbb{R}^{3 \times 3}$ can be expressed using the following similarity transformations

$${}^{\mathcal{W}}\mathbf{D} = {}^{\mathcal{W}}\mathbf{R}_H {}^{\mathcal{H}}\mathbf{D} {}^{\mathcal{H}}\mathbf{R}_W, \quad {}^{\mathcal{W}}\mathbf{E} = {}^{\mathcal{W}}\mathbf{R}_H {}^{\mathcal{H}}\mathbf{E} {}^{\mathcal{H}}\mathbf{R}_W. \quad (4)$$

In (4), the matrix ${}^{\mathcal{H}}\mathbf{R}_W$ represents the rotational transformation matrix from the inertial coordinate frame \mathcal{W} to the microswimmer coordinate frame \mathcal{H} . Furthermore,

the two constant matrices ${}^{\mathcal{H}}\mathbf{D}$, ${}^{\mathcal{H}}\mathbf{E}$, which depend on the microswimmer's physical parameters are given by

$${}^{\mathcal{H}}\mathbf{D} = \begin{bmatrix} \frac{1}{a_1} & 0 & 0 \\ 0 & \frac{1}{a_2} & 0 \\ 0 & 0 & \frac{1}{a_2} \end{bmatrix}, \quad {}^{\mathcal{H}}\mathbf{E} = \begin{bmatrix} -\frac{b_{11}}{a_1} & 0 & -\frac{b_{13}}{a_1} \\ 0 & -\frac{b_{22}}{a_2} & -\frac{b_{23}}{a_2} \\ 0 & \frac{b_{23}}{a_2} & -\frac{b_{33}}{a_2} \end{bmatrix}. \quad (5)$$

The dependency of the constant parameters in (5) in terms of the parameters of the microswimmer, i.e., ξ_{\parallel} , ξ_{\perp} , θ_h , r_h , n_h , and $|\mathbf{k}_h|$, are summarized in Table 1.

Remark 2.3 *As it can be seen from (3), one of the main challenges for closed-loop control of magnetic helical microswimmers is the need for sensing the orientation of the robot about its central axis $\mathbf{x}_{\mathcal{H}}$. However, under **H1** and **H2**, it is possible to simplify (3) in a way that there is no need for sensing the orientation of the microrobot.*

The following proposition summarizes the main results in [11]. One of the major implications of this proposition is removing the need for sensing the orientation of the microrobot about its central axis. Furthermore, this proposition gives the direction and magnitude of the feedforward angular velocity vector command input that results in a desired velocity vector for the magnetic microswimmer¹ (see Figure 1(c)).

Proposition 2.4 ([11]) *Consider the magnetic microswimmer dynamics given by (3). Under Hypotheses **H1** and **H2**, the dynamics of the helical microswimmer are equivalent to*

$$\dot{\mathbf{p}} = e_{11}\mathbf{u} + \mathbf{d}_{\mu}, \quad (6)$$

where

$$\dot{\mathbf{p}} := {}^{\mathcal{W}}\mathbf{v}, \quad \mathbf{u} := {}^{\mathcal{W}}\boldsymbol{\omega}, \quad \mathbf{d}_{\mu} := {}^{\mathcal{W}}\mathbf{D}{}^{\mathcal{W}}\mathbf{f}_d, \quad (7)$$

and

$$e_{11} = \frac{-2\pi n_h r_h^2 (\xi_{\parallel} - \xi_{\perp}) c_{\theta_h} s_{\theta_h}}{2\pi n_h r_h (\xi_{\parallel} c_{\theta_h}^2 + \xi_{\perp} s_{\theta_h}^2) + \xi_{vm} s_{\theta_h}}. \quad (8)$$

Furthermore, assume that the disturbance ${}^{\mathcal{W}}\mathbf{f}$ is contained in the plane spanned by \mathcal{P} and \mathbf{g} . Given a desired velocity vector \mathbf{v}^d in the plane spanned by \mathcal{P} and \mathbf{g} , the feedforward angular velocity command input \mathbf{u} , which makes the angle

$$\Psi = \arctan\left(\frac{\frac{1}{a_2} |\mathbf{f}_d| \sin(\alpha)}{|\mathbf{v}^d| + \frac{1}{a_2} |\mathbf{f}_d| \cos(\alpha)}\right), \quad (9)$$

¹ The authors in [11] provide their computational arguments in a Section entitled ‘‘Algorithm for Velocity Control with Gravity Compensation’’. For the reader’s convenience, we are succinctly presenting the computations and findings in [11] in the statement and proof of Proposition 2.4.

with \mathbf{v}^d and has the magnitude

$$|\mathbf{u}| = \frac{|\mathbf{v}^d| \cos(\Psi) + \frac{1}{a_1} |\mathbf{f}_d| \cos(\alpha - \Psi)}{e_{11}}, \quad (10)$$

yields the closed-loop dynamics

$$\dot{\mathbf{p}} = \mathbf{v}^d. \quad (11)$$

Proof. Under Hypothesis **H2**, we have $\mathbf{u} = \Omega \hat{\mathbf{k}}_h$. Also, the coordinates of the vector $\hat{\mathbf{k}}_h$ in the micro-robot frame \mathcal{H} are given by ${}^{\mathcal{H}}\hat{\mathbf{k}}_h = [1, 0, 0]^{\top}$ (see Figure 1(a)). Furthermore, from (5), it can be seen that ${}^{\mathcal{H}}\mathbf{E}{}^{\mathcal{H}}\hat{\mathbf{k}}_h = e_{11}{}^{\mathcal{H}}\hat{\mathbf{k}}_h$, where $e_{11} = \frac{-b_{11}}{a_1}$. Since

$${}^{\mathcal{W}}\mathbf{E}{}^{\mathcal{W}}\boldsymbol{\omega} = \Omega {}^{\mathcal{W}}\mathbf{E}{}^{\mathcal{W}}\hat{\mathbf{k}}_h = \Omega {}^{\mathcal{W}}\mathbf{R}_{\mathcal{H}}{}^{\mathcal{H}}\mathbf{E}{}^{\mathcal{H}}\mathbf{R}_{\mathcal{W}}{}^{\mathcal{W}}\hat{\mathbf{k}}_h =$$

$\Omega {}^{\mathcal{W}}\mathbf{R}_{\mathcal{H}}{}^{\mathcal{H}}\mathbf{E}{}^{\mathcal{H}}\hat{\mathbf{k}}_h = \Omega e_{11} {}^{\mathcal{W}}\mathbf{R}_{\mathcal{H}}{}^{\mathcal{H}}\hat{\mathbf{k}}_h = e_{11}(\Omega {}^{\mathcal{W}}\hat{\mathbf{k}}_h) = e_{11}\mathbf{u}$, the Equation given by (6) holds. Considering (6), it can be seen that the feedforward control law

$$\mathbf{u} = \frac{1}{e_{11}} \{ -\mathbf{d}_{\mu} + \mathbf{v}^d \}, \quad (12)$$

yields the closed-loop dynamics given by (11). Since \mathbf{f}_d is contained in $x_{\mathcal{H}} - z_{\mathcal{H}}$ plane (see Figure 1(c)), we have

$$\mathbf{f}_d = (\mathbf{f}_d \cdot \hat{\mathbf{k}}_h) \hat{\mathbf{k}}_h + (\mathbf{f}_d \cdot \hat{\mathbf{k}}_h^{\perp}) \hat{\mathbf{k}}_h^{\perp}. \quad (13)$$

Moreover, since the disturbance vector is contained in the plane spanned by \mathcal{P} and \mathbf{g} , ${}^{\mathcal{H}}\mathbf{f}_d = [\mathbf{f}_d \cdot \hat{\mathbf{k}}_h, \mathbf{f}_d \cdot \hat{\mathbf{k}}_h^{\perp}, 0]^{\top}$ holds in the coordinate frame \mathcal{H} . Hence, from (5), it can be seen that ${}^{\mathcal{H}}\mathbf{D}{}^{\mathcal{H}}\mathbf{f}_d = [\frac{1}{a_1} \mathbf{f}_d \cdot \hat{\mathbf{k}}_h, \frac{1}{a_2} \mathbf{f}_d \cdot \hat{\mathbf{k}}_h^{\perp}, 0]^{\top}$. Furthermore, we have $\mathbf{d}_{\mu} = {}^{\mathcal{W}}\mathbf{D}{}^{\mathcal{W}}\mathbf{f}_d = {}^{\mathcal{W}}\mathbf{R}_{\mathcal{H}}{}^{\mathcal{H}}\mathbf{D}{}^{\mathcal{H}}\mathbf{R}_{\mathcal{W}}{}^{\mathcal{W}}\mathbf{f}_d = {}^{\mathcal{W}}\mathbf{R}_{\mathcal{H}}{}^{\mathcal{H}}\mathbf{D}{}^{\mathcal{H}}\mathbf{f}_d$. Therefore, the vector \mathbf{d}_{μ} can be written as

$$\mathbf{d}_{\mu} = \frac{1}{a_1} (\mathbf{f}_d \cdot \hat{\mathbf{k}}_h) \hat{\mathbf{k}}_h + \frac{1}{a_2} (\mathbf{f}_d \cdot \hat{\mathbf{k}}_h^{\perp}) \hat{\mathbf{k}}_h^{\perp}. \quad (14)$$

Taking the dot product of \mathbf{d}_{μ} in (14) with $\hat{\mathbf{k}}_h$ and $\hat{\mathbf{k}}_h^{\perp}$ yields $\mathbf{d}_{\mu} \cdot \hat{\mathbf{k}}_h = \frac{1}{a_1} |\mathbf{f}_d| \cos(-\Psi + \alpha)$ and $\mathbf{d}_{\mu} \cdot \hat{\mathbf{k}}_h^{\perp} = \frac{1}{a_2} |\mathbf{f}_d| \cos(\frac{\pi}{2} - \Psi + \alpha)$, respectively (see Figure 1(c) for the angles Ψ and α). Also, $\mathbf{v}^d \cdot \hat{\mathbf{k}}_h = |\mathbf{v}^d| \cos(\Psi)$ and $\mathbf{v}^d \cdot \hat{\mathbf{k}}_h^{\perp} = |\mathbf{v}^d| \cos(\frac{\pi}{2} + \Psi)$. Since $\mathbf{u} = |\mathbf{u}| \hat{\mathbf{k}}_h$, taking the inner product of Equation (12) with $\hat{\mathbf{k}}_h$ yields

$$|\mathbf{u}| = \frac{1}{e_{11}} \left\{ \frac{1}{a_1} |\mathbf{f}_d| \cos(-\Psi + \alpha) + |\mathbf{v}^d| \cos(\Psi) \right\}. \quad (15)$$

Therefore, Equation (10) holds. Similarly, taking the inner product of Equation (12) with $\hat{\mathbf{k}}_h^{\perp}$ results in

$$0 = \frac{1}{e_{11}} \left\{ \frac{1}{a_2} |\mathbf{f}_d| \cos(\frac{\pi}{2} + \Psi - \alpha) + |\mathbf{v}^d| \cos(\frac{\pi}{2} + \Psi) \right\}. \quad (16)$$

Solving for Ψ from (15) and (16) will result in (9). ■

Table 1

The constant parameters in (5) in terms of physical characteristics of the magnetic helical microswimmer

Symbol	Description	Symbol	Description
a_1	$a_{h1} + \xi_{vm}$	a_2	$a_{h2} + \xi_{vm}$
a_{h1}	$\frac{2\pi n_h r_h (\xi_{\parallel} c_{\theta_h}^2 + \xi_{\perp} s_{\theta_h}^2)}{s_{\theta_h}}$	a_{h2}	$\frac{\pi n_h r_h (\xi_{\perp} + \xi_{\parallel} s_{\theta_h}^2 + \xi_{\perp} c_{\theta_h}^2)}{s_{\theta_h}}$
b_{11}	$2\pi n_h r_h^2 (\xi_{\parallel} - \xi_{\perp}) c_{\theta_h}$	b_{13}	$\frac{-b_{11}}{\tan(\theta_h)}$
b_{22}	$\frac{-3b_{11}}{4}$	b_{33}	$\frac{-b_{11}}{4}$
b_{23}	$\xi_{vm} \mathbf{k}_h $		

According to Proposition 2.4, which holds under **H1** and **H2**, we can constrain the motion of the magnetic microswimmer to the plane containing \mathcal{P} and \mathbf{g} by commanding the angular velocity vector $\boldsymbol{\omega}$ to be in this plane. Therefore, throughout the rest of the paper, we consider the motion of the helical microswimmer to be in the $\hat{\mathbf{e}}_x - \hat{\mathbf{e}}_z$ plane. Consequently, the position of the center of mass and the velocity of the microswimmer in the $\hat{\mathbf{e}}_x - \hat{\mathbf{e}}_z$ plane are given by $\mathbf{p} = [p_x, p_z]^\top$ and $\mathbf{v} = \dot{\mathbf{p}}$, respectively, where $\mathbf{v} = [v_x, v_z]^\top$. We denote the angle of the center of mass (COM) position vector in the $\hat{\mathbf{e}}_x - \hat{\mathbf{e}}_z$ plane by θ . Therefore,

$$\theta := \text{atan2}(p_z, p_x). \quad (17)$$

Remark 2.5 Under **H2**, we can directly command $\boldsymbol{\omega}$, which is aligned with the axis of the helical microrobot, and hence there is no need for measuring the orientation of the helical microswimmer. The only required measurements for implementing our proposed control laws are the COM Cartesian coordinates given by p_x and p_z . The angle θ in (17) and the magnitude $|\mathbf{p}|$ are the polar coordinates of the position vector $\mathbf{p} = [p_x, p_z]^\top$.

3 Control Problem Formulation and Solution Strategy

In this section we formulate the straight-line path following control problem for swimming magnetic helical microrobots and outline our solution strategy.

Before stating the control objective, we introduce a coordinate transformation that maps the position of the microswimmer's COM to the cross-track error to the path and the projected position along the path, respectively. In particular, given the straight line \mathcal{P} in (1) and assuming that it makes the angle θ_r with $\hat{\mathbf{e}}_x$ (see Figure 1(a)), we define the cross-track error to \mathcal{P} as

$$\varepsilon := \hat{\mathbf{e}}_{\theta_r}^\perp \mathbf{p}, \quad (18)$$

where

$$\hat{\mathbf{e}}_{\theta_r}^\perp := \begin{bmatrix} -\sin(\theta_r) \\ \cos(\theta_r) \end{bmatrix}, \quad (19)$$

is the unit vector perpendicular to \mathcal{P} . We also define the projected position along the path as

$$z := \hat{\mathbf{e}}_{\theta_r}^\top \mathbf{p}, \quad (20)$$

where

$$\hat{\mathbf{e}}_{\theta_r}^\top := \begin{bmatrix} \cos(\theta_r) \\ \sin(\theta_r) \end{bmatrix}, \quad (21)$$

is the unit vector parallel to the line \mathcal{P} . When $\varepsilon = 0$, the variable z provides the position of the microswimmer along \mathcal{P} . From (17), it can be seen that $p_x = |\mathbf{p}| \cos(\theta)$ and $p_z = |\mathbf{p}| \sin(\theta)$. Hence, we can rewrite the cross-track error as $\varepsilon = \hat{\mathbf{e}}_{\theta_r}^\perp \mathbf{p} = [-\sin(\theta_r)p_x + \cos(\theta_r)p_z] = |\mathbf{p}| [\sin(\theta) \cos(\theta_r) - \cos(\theta) \sin(\theta_r)]$. Since $\sin(\theta - \theta_r) = \sin(\theta) \cos(\theta_r) - \cos(\theta) \sin(\theta_r)$, we have

$$\varepsilon = |\mathbf{p}| \sin(\Delta\theta), \quad (22)$$

where $\Delta\theta := \theta - \theta_r$. Similarly, it can be shown that

$$z = |\mathbf{p}| \cos(\Delta\theta). \quad (23)$$

Straight-Line Path Following Control (LFC) Problem. Consider a given step-out frequency $\Omega_{SO} > 0$ and the straight line \mathcal{P} given by (1). Consider the planar magnetic microswimmer whose dynamics are given by (6). Assume that the disturbance input $\mathbf{d}_\mu : \mathbb{R}_+ \rightarrow \mathbb{R}^2$ in (7) is piecewise continuous and satisfies $\|\mathbf{d}_\mu\|_\infty < d^*$ for a positive, yet unknown, d^* . Make the cross-track error ε in (22) to practically converge² to \mathcal{P} with a continuous and bounded velocity profile $\dot{\mathbf{p}}(t)$ such that $|\mathbf{u}(t)| \leq \Omega_{SO}$ for all $t \geq 0$.

Remark 3.1 In both the work of Mahoney et al. [11] and our prior work in [15], it is assumed that the only disturbance acting on the microswimmer is the weight of the microrobot and its magnitude is known. In this paper, we remove this requirement.

Solution Strategy. Our solution to microrobot LFC problem unfolds in the following steps.

² Practical stabilization of a variable means that by a suitable choice of controller parameters the variable is made to converge to an arbitrarily small neighborhood of its desired value.

Step 1: In Section 4.1, we consider the reference model

$$\dot{\mathbf{p}} = \mathbf{v}^d(\mathbf{p}, s), \quad (24)$$

where $\mathbf{v}^d(\mathbf{p}, s)$ is the desired closed-loop vector field coming from an ILOS guidance law, which depends on a dynamic variable s . In Step 1, we prove that the LFC problem objective is achieved when the velocity command input \mathbf{u} is set equal to the reference vector field in (24) in the absence of disturbances and step-out frequency constraints. Furthermore, we show that under bounded disturbances the cross-track error and the dynamic variable s in the ILOS guidance law remain bounded.

Step 2: Having obtained a desired closed loop vector field that achieves the LFC objective in Step 1, we cast the control problem as an ODS-based quadratic program over a sphere in Section 4.2. This ODS-based quadratic program minimizes, at each position \mathbf{p} , the difference between the open-loop and the reference model vector fields in (24), while respecting the step-out frequency constraints on the angular velocity command inputs. In this step, we provide closed-form solutions for the ODS-based QP and give sufficient conditions under which the generated angular velocity command input is smooth.

4 Straight-Line Path Following Control Problem Solution

In order to solve LFC problem, we proceed according to the solution strategy outlined in the previous section.

4.1 Step 1: Integral line-of-sight reference vector field

Considering the path \mathcal{P} in (1), we propose a reference vector field for the closed-loop dynamics that achieves the LFC problem objective. This vector field is inspired from the ILOS path following laws for underactuated marine craft control (see, e.g., [36]). In ILOS-based guidance schemes, the cross-track error of the moving object to the desired path is minimized while the controlled object is pointing at a moving target point on the desired path (see Figure 2(a)). In addition to the cross track-error to \mathcal{P} , ILOS-based guidance laws incorporate the integral of the cross-track error using a dynamic variable s . In the presence of disturbances that drive the microswimmer away from its desired path, embedding the integral compensation dynamics via the dynamic variable s will build up a corrective action in the reference vector field. Given the LFC problem for the magnetic microswimmer, we propose the following ILOS reference vector field

$$\mathbf{v}^d(\mathbf{p}, s) = \alpha_d \mathbf{R}_{\theta_r} \begin{bmatrix} \Delta_{\text{LOS}} \\ -|\mathbf{p}| \sin(\Delta\theta) - \sigma_0 s \end{bmatrix}, \quad (25)$$

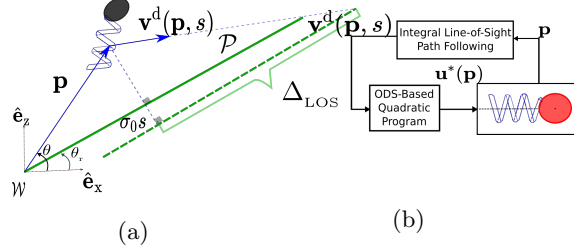


Fig. 2. (a) Integral line-of-sight reference vector field and (b) block diagram of the ODS-based control scheme.

where $\alpha_d > 0$ and the integral gain $\sigma_0 > 0$ are constant design parameters, \mathbf{p} is the position of the center of mass of the microrobot with respect to the inertial frame \mathcal{W} , and the matrix \mathbf{R}_{θ_r} is the rotation matrix by θ_r . The parameter $\Delta_{\text{LOS}} > 0$, which determines the point along \mathcal{P} at which the microrobot should be pointed (see Figure 2(a)), is called the *look-ahead distance*. Furthermore, s is a dynamic variable whose dynamics are governed by

$$\dot{s} = -k_d s + \Delta_{\text{LOS}} \frac{|\mathbf{p}| \sin(\Delta\theta)}{(|\mathbf{p}| \sin(\Delta\theta) + \sigma_0 s)^2 + \Delta_{\text{LOS}}^2}, \quad (26)$$

where the damping gain $k_d > 0$ is a constant design parameter. Figure 2(a) provides the geometric interpretation of the proposed ILOS guidance law in (25) and (26). The idea behind (25) and (26) is that the integral of the cross-track error $\varepsilon = |\mathbf{p}| \sin(\Delta\theta)$ will allow the angle between $\mathbf{v}^d(\mathbf{p}, s)$ and \mathcal{P} to be non-zero when $\varepsilon = 0$, i.e., when the microswimmer is moving on the desired line. In particular, in the presence of disturbances driving the microswimmer away from its path, the integral of the cross-track error will build up to create a non-zero side-slip angle to follow the line.

We can rewrite the ILOS reference vector field in (25) and (26) in terms of the cross-track error given by (22) as

$$\mathbf{v}^d(\varepsilon, s) = \alpha_d \mathbf{R}_{\theta_r} \begin{bmatrix} \Delta_{\text{LOS}} \\ -\varepsilon - \sigma_0 s \end{bmatrix}, \quad (27)$$

$$\dot{s} = -k_d s + \Delta_{\text{LOS}} \frac{\varepsilon}{(\varepsilon + \sigma_0 s)^2 + \Delta_{\text{LOS}}^2}.$$

We now derive the closed-loop dynamics of the cross-track error under the effect of disturbances while assuming that there are no restrictions on the control input magnitude. In the next section, we formally take into account the angular velocity command input restrictions due to the step-out frequency constraint.

Considering the microswimmer's dynamics in (6), an estimate \hat{e}_{11} of the physical parameter e_{11} in (8) and an estimate $\hat{\mathbf{d}}_\mu$ of the disturbance vector \mathbf{d}_μ in (7), and assuming that the control input has been chosen to be

$$\mathbf{u} = \frac{1}{\hat{e}_{11}} \mathbf{v}^d - \frac{1}{\hat{e}_{11}} \hat{\mathbf{d}}_\mu, \quad (28)$$

we get the closed-loop dynamics

$$\dot{\mathbf{p}} = \frac{e_{11}}{\hat{e}_{11}} \mathbf{v}^d + \mathbf{d}_\mu - \frac{e_{11}}{\hat{e}_{11}} \hat{\mathbf{d}}_\mu. \quad (29)$$

Remark 4.1 *If no knowledge of e_{11} and \mathbf{d}_μ are available, one can choose the estimates $\hat{e}_{11} = 1$ and $\hat{\mathbf{d}}_\mu = \mathbf{0}$ in (28). In deriving the cross-track error dynamics under ILOS-based guidance laws and their stability properties, we assume that $\hat{e}_{11} = 1$ and $\hat{\mathbf{d}}_\mu = \mathbf{0}$.*

Therefore, the dynamics of the cross-track error in (22) under the control law in (28) are given by

$$\dot{\varepsilon} = e_{11} \alpha_d \hat{\mathbf{e}}_{\theta_r}^{\perp \top} \dot{\mathbf{p}} = \alpha_d \hat{\mathbf{e}}_{\theta_r}^{\perp \top} \left(\frac{e_{11}}{\hat{e}_{11}} \mathbf{v}^d + \mathbf{d}_\mu - \frac{e_{11}}{\hat{e}_{11}} \hat{\mathbf{d}}_\mu \right). \quad (30)$$

Using the ILOS guidance law $\mathbf{v}^d = \mathbf{v}^d(\varepsilon, s)$ in (27), assuming $\hat{e}_{11} = 1$ and $\hat{\mathbf{d}}_\mu = \mathbf{0}$ (see Remark 4.1), and noticing that $\hat{\mathbf{e}}_{\theta_r}^{\perp \top} \mathbf{R}_{\theta_r} = [0, 1]$, we obtain

$$\dot{\varepsilon} = \alpha_d e_{11} (-\varepsilon - \sigma_0 s) + \alpha_d d_\mu^\perp, \quad (31)$$

where $d_\mu^\perp := \hat{\mathbf{e}}_{\theta_r}^{\perp \top} \mathbf{d}_\mu$. Similarly, the dynamics of z defined in (20) are found to be

$$\dot{z} = e_{11} \alpha_d \Delta_{\text{LOS}} + \alpha_d d_\mu^\parallel,$$

where $d_\mu^\parallel := \hat{\mathbf{e}}_{\theta_r}^\top \mathbf{d}_\mu$. Consequently, the closed-loop dynamics of the helical microswimmer under the control law (28) with $\hat{e}_{11} = 1$ and $\hat{\mathbf{d}}_\mu = \mathbf{0}$ (see Remark 4.1) and the ILOS guidance law $\mathbf{v}^d = \mathbf{v}^d(\varepsilon, s)$ in (27) are governed by

$$\begin{aligned} \dot{\varepsilon} &= -\alpha_d \varepsilon - \alpha_d \sigma_0 s + \alpha_d d_\mu^\perp, \\ \dot{s} &= -k_d s + \Delta_{\text{LOS}} \frac{\varepsilon}{(\varepsilon + \sigma_0 s)^2 + \Delta_{\text{LOS}}^2}, \\ \dot{z} &= \alpha_d e_{11} \Delta_{\text{LOS}} + \alpha_d d_\mu^\parallel. \end{aligned} \quad (32)$$

Remark 4.2 *As it can be seen from Equation (32), the dynamics of s have the property that $\dot{s} \rightarrow -k_d s$ as $\varepsilon \rightarrow \infty$, implying that the rate of integration will decrease with large cross-track errors. In particular, the integral term will be less dominant when the cross-track error is large, i.e., when the microswimmer is far from the desired line \mathcal{P} . As stated in [36], such error-dependent attenuation of integral action will reduce the risk of integrator wind-up and its resulting performance limitations.*

In order to investigate the stability properties of the cross-track error dynamics in (32), we define the following state and disturbance vectors

$$\mathbf{x} := \begin{bmatrix} \varepsilon \\ s \end{bmatrix}, \quad \mathbf{d}_\mu^\perp := \begin{bmatrix} d_\mu^\perp \\ 0 \end{bmatrix}. \quad (33)$$

Using (32), the dynamics of \mathbf{x} can be written as

$$\dot{\mathbf{x}} = \mathbf{A} \mathbf{x} + \mathbf{G}(\mathbf{x}) \mathbf{x} + \alpha_d \mathbf{d}_\mu^\perp, \quad (34)$$

where

$$\begin{aligned} \mathbf{A} &:= -\alpha_d \begin{bmatrix} 1 & \sigma_0 \\ 0 & \frac{k_d}{\alpha_d} \end{bmatrix}, \quad \mathbf{G}(\mathbf{x}) := \frac{\Delta_{\text{LOS}}}{\mathbf{x}^\top \mathbf{H} \mathbf{x} + \Delta_{\text{LOS}}^2} \mathbf{B}, \\ \mathbf{H} &:= \begin{bmatrix} 1 & \sigma_0 \\ \sigma_0 & \sigma_0^2 \end{bmatrix}, \quad \mathbf{B} := \begin{bmatrix} 0 & 0 \\ 1 & 0 \end{bmatrix}. \end{aligned} \quad (35)$$

The following proposition describes the stability properties of the cross-track error dynamics in (34) and (35) as well as the steady-state velocity along \mathcal{P} .

Proposition 4.3 *Consider the helical microswimmer dynamics in (6) under the angular velocity control input (28) with $\hat{e}_{11} = 1$, $\hat{\mathbf{d}}_\mu = \mathbf{0}$, and the ILOS guidance law $\mathbf{v}^d = \mathbf{v}^d(\mathbf{p}, s)$ given by (25) and (26). Suppose that there exist symmetric positive definite matrices $\mathbf{\Gamma}$ and*

$$\mathbf{P} = \begin{bmatrix} p_{11} & p_{12} \\ p_{12} & p_{22} \end{bmatrix} \quad \text{such that}$$

$$\begin{aligned} \mathbf{A}^\top \mathbf{P} + \mathbf{P} \mathbf{A} &= -\mathbf{\Gamma}, \\ \lambda_{\min}(\mathbf{\Gamma}) &> \frac{p_{12} + \sqrt{p_{12}^2 + p_{22}^2}}{\Delta_{\text{LOS}}}. \end{aligned} \quad (36)$$

Then, under $d_\mu^\perp = 0$, the cross-track error dynamics in (34) are globally exponentially stable (GES). Moreover, if $d_\mu^\parallel = 0$, $\dot{\mathbf{p}}(t) \rightarrow e_{11} \alpha_d \Delta_{\text{LOS}} \hat{\mathbf{e}}_{\theta_r}$ as $t \rightarrow \infty$. Furthermore, if $\lambda_{\min}(\mathbf{\Gamma}) > \frac{p_{12}}{\Delta_{\text{LOS}}} + \sqrt{p_{12}^2 + p_{22}^2} (\alpha_d + \frac{1}{\Delta_{\text{LOS}}})$, the cross-track error dynamics in (34) are input-to-state stable (ISS). Consequently, if $\|\mathbf{d}_\mu\|_\infty < d^$ for some constant $d^* > 0$, then $[\varepsilon, s]^\top$ will converge to the ball $\mathcal{B}_{d^* \lambda_{\max}(\mathbf{P}) / \lambda_{\min}(\mathbf{P})}(\mathbf{0})$.*

Proof. Consider the quadratic Lyapunov function candidate

$$V(\mathbf{x}) := \mathbf{x}^\top \mathbf{P} \mathbf{x}, \quad (37)$$

and compute its derivative $\dot{V}(\mathbf{x}) := \frac{\partial V}{\partial \mathbf{x}} \dot{\mathbf{x}}$ along the trajectories of the error dynamics in (34) to obtain

$$\begin{aligned} \dot{V}(\mathbf{x}) &= \mathbf{x}^\top (\mathbf{A}^\top \mathbf{P} + \mathbf{P} \mathbf{A}) \mathbf{x} + \frac{\Delta_{\text{LOS}}}{\mathbf{x}^\top \mathbf{H} \mathbf{x} + \Delta_{\text{LOS}}^2} \mathbf{x}^\top (\mathbf{B}^\top \mathbf{P} + \\ &\quad \mathbf{P} \mathbf{B}) \mathbf{x} + 2\alpha_d \mathbf{x}^\top \mathbf{P} \mathbf{d}_\mu^\perp. \end{aligned} \quad (38)$$

Using the Rayleigh's inequality, we have $\dot{V}(\mathbf{x}) \leq -\lambda_{\min}(\mathbf{\Gamma}) |\mathbf{x}|^2 + \frac{\Delta_{\text{LOS}} \lambda_{\max}(\mathbf{B}^\top \mathbf{P} + \mathbf{P} \mathbf{B})}{\lambda_{\min}(\mathbf{H}) |\mathbf{x}|^2 + \Delta_{\text{LOS}}^2} |\mathbf{x}|^2 + 2\alpha_d \mathbf{x}^\top \mathbf{P} \mathbf{d}_\mu^\perp$. Since $\lambda_{\min}(\mathbf{H}) = 0$, $\lambda_{\max}(\mathbf{B}^\top \mathbf{P} + \mathbf{P} \mathbf{B}) = p_{12} +$

$\sqrt{p_{12}^2 + p_{22}^2}$, and from (36), it can be seen that

$$\dot{V}(x) \leq -\left(\lambda_{\min}(\mathbf{\Gamma}) - \frac{p_{12} + \sqrt{p_{12}^2 + p_{22}^2}}{\Delta_{\text{LOS}}}\right)|\mathbf{x}|^2 + 2\alpha_d \mathbf{x}^\top \mathbf{P} \mathbf{d}_\mu^\perp. \quad (39)$$

Hence, $V(\mathbf{x})$ in (37) is a Lyapunov function for the cross-track error dynamics, which satisfies $\frac{1}{2}\lambda_{\min}(\mathbf{P})|\mathbf{x}|^2 \leq V(\mathbf{x}) \leq \frac{1}{2}\lambda_{\max}(\mathbf{P})|\mathbf{x}|^2$ for all \mathbf{x} . Additionally, since $V(\mathbf{x})$ is radially unbounded (i.e., $V(\mathbf{x}) \rightarrow \infty$ as $|\mathbf{x}| \rightarrow \infty$), when $\mathbf{d}_\mu^\perp = \mathbf{0}$, the origin $\mathbf{x} = \mathbf{0}$ is globally exponentially stable (GES) for the cross-track error dynamics (see Theorem 4.10 in [41]). Furthermore, since $[\varepsilon, s]^\top \rightarrow \mathbf{0}$ as $t \rightarrow \infty$, we have $\Delta\theta = 0$. Therefore, on \mathcal{P} where $\varepsilon = 0$, it can be seen that

$$\mathbf{v}^d(\mathbf{p}, 0) \Big|_{\mathbf{p} \in \mathcal{P}} = \alpha_d \mathbf{R}_{\theta_r} \begin{bmatrix} \Delta_{\text{LOS}} \\ 0 \end{bmatrix} = \alpha_d \Delta_{\text{LOS}} \hat{\mathbf{e}}_{\theta_r}. \quad (40)$$

Consequently, using (40) in (29) when $d_\mu^\parallel = d_\mu^\perp = 0$, it can be seen that $\dot{\mathbf{p}}(t) \rightarrow e_{11}\alpha_d\Delta_{\text{LOS}}\hat{\mathbf{e}}_{\theta_r}$ as $[\varepsilon, s]^\top \rightarrow \mathbf{0}$ when $t \rightarrow \infty$. Since the derivative of the quadratic Lyapunov function $V(\mathbf{x})$ in (37) along the trajectories of the cross-track error dynamics satisfies $\dot{V}(x) \leq -\left(\lambda_{\min}(\mathbf{\Gamma}) - \frac{p_{12} + \sqrt{p_{12}^2 + p_{22}^2}}{\Delta_{\text{LOS}}} - \sqrt{p_{12}^2 + p_{22}^2}\alpha_d\right)|\mathbf{x}|^2$, for all $|\mathbf{x}| \geq \|\mathbf{d}_\mu^\perp\|_\infty$. Therefore, if $\lambda_{\min}(\mathbf{\Gamma}) > \frac{p_{12}}{\Delta_{\text{LOS}}} + \sqrt{p_{12}^2 + p_{22}^2}\left(\alpha_d + \frac{1}{\Delta_{\text{LOS}}}\right)$, the closed-loop dynamics are ISS and convergence to $\mathcal{B}_{d^* \lambda_{\max}(\mathbf{P})/\lambda_{\min}(\mathbf{P})}(\mathbf{0})$ holds (see Theorem 4.19 in [41]). ■

The following corollary follows from Proposition 4.3.

Corollary 4.4 *Assume the conditions in Proposition 4.3. Then, under $\mathbf{d}_\mu = \mathbf{0}$, the set $\mathcal{P} \times \{s = 0\}$ is an invariant set for the microswimmer closed-loop dynamics under the control law (28) with $\hat{e}_{11} = 1$, $\hat{\mathbf{d}}_\mu = \mathbf{0}$, and the ILOS guidance law $\mathbf{v}^d = \mathbf{v}^d(\mathbf{p}, s)$ given by (25) and (26). Furthermore, once the path \mathcal{P} in (1) is made invariant, the speed of the microswimmer along \mathcal{P} is*

$$v^* = e_{11}\alpha_d\Delta_{\text{LOS}}. \quad (41)$$

It is possible to further simplify the conditions in (36) in a way that we obtain inequality constraints on the design parameters k_d , α_d , σ_0 , and Δ_{LOS} . First, it can be shown that the roots r_i , $i = 1, 2$, of the quadratic polynomial $P(\lambda) = \lambda^2 - \left(\frac{k_d}{\alpha_d} + \frac{p_{11}}{p_{12}} + \frac{\sigma_0 p_{22}}{p_{12}}\right)\lambda + \frac{\sigma_0 p_{11} p_{22}}{p_{12}^2} - \frac{1}{4}\left(\frac{\sigma_0 p_{11}}{p_{12}} + \left(1 + \frac{k_d}{\alpha_d} \frac{p_{22}}{p_{12}}\right)^2\right)$ satisfy the relationship $\lambda_{i\Gamma} = 2\alpha_d p_{12} r_i$, $i = 1, 2$ with $\lambda_{i\Gamma}$ being the eigenvalues of $\mathbf{\Gamma}$ in (36). Next, by computing the eigenvalues of $\mathbf{\Gamma}$ via finding the roots of $P(\cdot)$ and under the simplifying assumption $p_{11} = p_{22}$,

it can be shown that the two inequalities

$$\frac{k_d}{\alpha_d} \geq 0, \quad (\sigma_0 \alpha_d \Delta_{\text{LOS}})^2 + 2\alpha_d \Delta_{\text{LOS}} \left(1 + \frac{k_d}{\alpha_d}\right) \leq 1 \quad (42)$$

guarantee that the conditions in (36) are satisfied.

4.2 Step 2: ODS-based quadratic program

In this section, we present a feedback control solution for the microrobot LFC problem based on the optimal decision strategy (ODS) framework [34]. Considering the ILOS-based reference vector field in (25) and (26), it is clear from Proposition 4.3 that if the control input \mathbf{u} is designed such that the closed-loop dynamics are driven by the ILOS-based guidance law, then the LFC problem objective is achieved. However, the step-out frequency limitation

$$|\mathbf{u}(t)| \leq \Omega_{\text{SO}}, \quad (43)$$

on the rotational frequency of the helical microswimmer about its axis constrains the magnitude of the angular velocity command input \mathbf{u} . Using the ODS framework, we will address this constraint.

ODS-based control is a pointwise optimal control solution that, in the context of our problem, minimizes the deviation between the vector field of the microswimmer open-loop dynamics in (6) and the ILOS-based reference vector field in (25) and (26), while respecting the step-out frequency constraint in (43). In order to state the ODS-based control scheme for the microswimmer, let $\mathbf{p}(t, t_0, \mathbf{p}_0, \mathbf{u}(t))$, or $\mathbf{p}(t, \mathbf{u}(t))$ or $\mathbf{p}(t)$ for short, denote the solution to (6) corresponding to the control input $t \mapsto \mathbf{u}(t)$ and initial position \mathbf{p}_0 at time t_0 . For each solution $\mathbf{p}(t)$, we define the set of permissible velocity vectors C_t to be the translation by $\mathbf{p}(t)$ of the set

$$C(\mathbf{p}(t)) := \{\mathbf{v}(t, \mathbf{w}) \in \mathbb{R}^2 \mid \mathbf{v} = \mathbf{d}_\mu + e_{11}\mathbf{w}, |\mathbf{w}| \leq \Omega_{\text{SO}}\}. \quad (44)$$

Therefore, for any control input $\mathbf{u}(t)$ that respects the step-out frequency constraint in (43), the velocity of the microswimmer lies in the set $C(\mathbf{p}(t))$ (see Figure 3).

In the case of the microrobot LFC, we choose the ODS-based control law $\mathbf{u}(t)$ in a way that at each time t , the instantaneous velocity of the microswimmer is “nearest” to the ILOS-based guidance law $\mathbf{v}^d(\mathbf{p}(t), s(t))$ given by (25), (26) in the norm on \mathbb{R}^2 defined by some positive definite matrix \mathbf{Q} . In other words, the ODS-based control law at each t is the minimizing solution to

$$\min_{\mathbf{v} \in C(\mathbf{p}(t))} \left\{ \left[\mathbf{v} - \mathbf{v}^d(\mathbf{p}(t), s(t)) \right]^\top \mathbf{Q} \left[\mathbf{v} - \mathbf{v}^d(\mathbf{p}(t), s(t)) \right] \right\}. \quad (45)$$

The minimization problem in (45) is equivalent to the

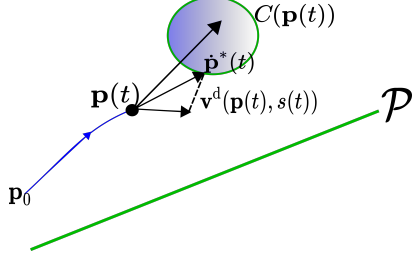


Fig. 3. Geometric interpretation of optimal decision strategy.

explicit minimization in $\mathbf{u}(t)$,

$$\min_{\mathbf{u}} \left\{ \left[e_{11} \mathbf{u}(t) + \mathbf{d}_\mu(t) - \mathbf{v}^d(\mathbf{p}(t), s(t)) \right]^\top \mathbf{Q} \left[e_{11} \mathbf{u}(t) + \mathbf{d}_\mu(t) - \mathbf{v}^d(\mathbf{p}(t), s(t)) \right] \right\} \quad (46)$$

subject to $|\mathbf{u}(t)| \leq \Omega_{SO}$,

which, in turn, can be shown to be equivalent to the QP

$$\min_{\mathbf{u}} \left\{ \frac{1}{2} \mathbf{u}^\top \mathbf{A}_\mu \mathbf{u} + \mathbf{G}_\mu^\top(\mathbf{p}, s) \mathbf{u} \right\} \quad (47)$$

subject to $\mathbf{u}^\top \mathbf{u} \leq \Omega_{SO}^2$,

where

$$\begin{aligned} \mathbf{A}_\mu &:= e_{11}^2 \mathbf{Q}, \\ \mathbf{G}_\mu(\mathbf{p}, s) &:= \frac{-\mathbf{A}_\mu}{e_{11}} (\mathbf{d}_\mu - \mathbf{v}^d(\mathbf{p}, s)), \end{aligned} \quad (48)$$

The QP in (47), which involves minimizing a quadratic over a sphere, is called a trust region subproblem (TRS) [38]. It is well-known from the TRS literature (see, e.g., Theorem 1.1 in [37]) that \mathbf{u} is a solution to the TRS in (47) *if and only if* there exists $\lambda^* \geq 0$ such that

$$|\mathbf{u}^*| \leq \Omega_{SO}, \quad (49a)$$

$$(\mathbf{A}_\mu + \lambda^* \mathbf{I}) \mathbf{u}^* = -\mathbf{G}_\mu(\mathbf{p}, s), \quad (49b)$$

$$\lambda^* (\Omega_{SO} - |\mathbf{u}^*|) = 0, \quad (49c)$$

$$\mathbf{A}_\mu + \lambda^* \mathbf{I} \succeq \mathbf{0}. \quad (49d)$$

Using proper state transformations, it is possible to restate the ODS problem in (46) such that \mathbf{Q} becomes diagonal. In the rest of this paper and without loss of generality, we assume that \mathbf{Q} in the ODS problem in (46) has the diagonal form $\mathbf{Q} = \text{diag}\{q_1, q_2\}$, where $q_1 > 0$ and $q_2 > 0$ are design parameters. The following proposition provides the solutions to the TRS in (47) and (48).

Proposition 4.5 *Consider the QP in (47) with the matrix $\mathbf{Q} = \text{diag}\{q_1, q_2\}$. Then, the optimal pointwise angular velocity control input, which solves (47), is given by*

$$\mathbf{u}^*(\mathbf{p}, s) = \begin{cases} -\mathbf{A}_\mu^{-1} \mathbf{G}_\mu(\mathbf{p}, s) & \text{if } |\mathbf{u}^*| < \Omega_{SO} \\ -(\mathbf{A}_\mu + \lambda^* \mathbf{I})^{-1} \mathbf{G}_\mu(\mathbf{p}, s) & \text{if } |\mathbf{u}^*| = \Omega_{SO} \end{cases} \quad (50)$$

where \mathbf{A}_μ and $\mathbf{G}_\mu(\mathbf{p}, s) = [G_{1\mu}(\mathbf{p}, s), G_{2\mu}(\mathbf{p}, s)]^\top$ are defined in (48), and λ^* is a non-negative root to the following algebraic equation

$$\frac{G_{1\mu}^2(\mathbf{p}, s)}{(e_{11}^2 q_1 + \lambda^*)^2} + \frac{G_{2\mu}^2(\mathbf{p}, s)}{(e_{11}^2 q_2 + \lambda^*)^2} = \Omega_{SO}^2. \quad (51)$$

Furthermore, the angular velocity control input $\mathbf{u}^*(\mathbf{p})$ will be absolutely continuous if and only if $q_1 = q_2 = \frac{1}{\Omega_0 e_{11}^2}$ for some $\Omega_0 > 0$, and given by

$$\mathbf{u}^*(\mathbf{p}, s) = \begin{cases} -\Omega_0 \mathbf{G}_\mu(\mathbf{p}, s) & \text{if } |\mathbf{G}_\mu(\mathbf{p}, s)| < \frac{\Omega_{SO}}{\Omega_0} \\ -\Omega_{SO} \frac{\mathbf{G}_\mu(\mathbf{p}, s)}{|\mathbf{G}_\mu(\mathbf{p}, s)|} & \text{if } |\mathbf{G}_\mu(\mathbf{p}, s)| \geq \frac{\Omega_{SO}}{\Omega_0} \end{cases} \quad (52)$$

Proof. Consider the necessary and sufficient conditions in (49). Suppose that $|\mathbf{u}^*| < \Omega_{SO}$. Then, according to (49c), $\lambda^* = 0$. Hence, under $|\mathbf{u}^*| < \Omega_{SO}$ and from (49b), it can be seen that $\mathbf{u}^*(\mathbf{p}, s) = -\mathbf{A}_\mu^{-1} \mathbf{G}_\mu(\mathbf{p}, s)$. Next, suppose $|\mathbf{u}^*| = \Omega_{SO}$. From (49b), it follows that

$$\mathbf{u}^* = -(\mathbf{A}_\mu + \lambda^* \mathbf{I})^{-1} \mathbf{G}_\mu(\mathbf{p}, s). \quad (53)$$

In order to find the constant λ^* in the previous equation, we use (53) to get

$$\mathbf{u}^{*\top} \mathbf{u}^* = \mathbf{G}_\mu(\mathbf{p}, s)^\top (\mathbf{A}_\mu + \lambda^* \mathbf{I})^{-2} \mathbf{G}_\mu(\mathbf{p}, s). \quad (54)$$

Since

$$(\mathbf{A}_\mu + \lambda^* \mathbf{I})^{-1} \mathbf{G}_\mu(\mathbf{p}, s) = \begin{bmatrix} \frac{G_{1\mu}(\mathbf{p}, s)}{e_{11}^2 q_1 + \lambda^*} \\ \frac{G_{2\mu}(\mathbf{p}, s)}{e_{11}^2 q_2 + \lambda^*} \end{bmatrix}, \quad (55)$$

the right hand side of the equation in (54) is equal to $\frac{G_{1\mu}^2(\mathbf{p}, s)}{(e_{11}^2 q_1 + \lambda^*)^2} + \frac{G_{2\mu}^2(\mathbf{p}, s)}{(e_{11}^2 q_2 + \lambda^*)^2}$. Therefore, since $\mathbf{u}^{*\top} \mathbf{u}^* = \Omega_{SO}^2$, the constant λ^* satisfies (54) if the algebraic equation in (51) holds. Next, we define

$$\tilde{\lambda} := \lambda^* + \Omega_1, \tilde{\Omega} := \Omega_2 - \Omega_1, \Omega_1 := q_1 e_{11}^2, \text{ and } \Omega_2 := q_2 e_{11}^2. \quad (56)$$

Using the definitions in (56), the algebraic equation in (51) can be transformed into the following equivalent quartic equation

$$\tilde{\lambda}^4 + 2\tilde{\Omega}\tilde{\lambda}^3 - \left[\frac{|\mathbf{G}_\mu(\mathbf{p}, s)|^2}{\Omega_{SO}^2} - \tilde{\Omega}^2 \right] \tilde{\lambda}^2 - 2\tilde{\Omega} G_{1\mu}^2(\mathbf{p}, s) \tilde{\lambda} - \tilde{\Omega}^2 = 0. \quad (57)$$

Also, using the definitions in (56), the control input given by (50) can be further simplified to

$$\mathbf{u}^*(\mathbf{p}, s) = \begin{cases} -\left[\frac{G_{1\mu}(\mathbf{p}, s)}{\Omega_1}, \frac{G_{2\mu}(\mathbf{p}, s)}{\Omega_2} \right]^\top & \text{if } |\mathbf{u}^*(\mathbf{p}, s)| < \Omega_{SO} \\ -\left[\frac{G_{1\mu}(\mathbf{p}, s)}{\lambda_0}, \frac{G_{2\mu}(\mathbf{p}, s)}{\lambda_0 + \tilde{\Omega}} \right]^\top & \text{if } |\mathbf{u}^*(\mathbf{p}, s)| = \Omega_{SO} \end{cases} \quad (58)$$

where $\tilde{\lambda}_0$ is a root of the quartic equation in (57). From a standard continuity argument, it can be deduced that $\mathbf{u}^*(\cdot)$ is continuous for every $\mathbf{p} \in \mathbb{R}^2$ if and only if

$$\tilde{\lambda}_0 = \Omega_1. \quad (59)$$

Hence the pointwise optimal control input $\mathbf{u}^*(\cdot)$ is continuous everywhere if and only if

$$\lambda^* = 0. \quad (60)$$

Therefore, $q_1 = q_2 = \frac{1}{\Omega_0 e_{11}^2}$, for some $\Omega_0 > 0$. Consequently, the equation in (51) gets reduced to

$$G_{1\mu}(\mathbf{p}, s)^2 + G_{2\mu}(\mathbf{p}, s)^2 = (\lambda^* + \frac{1}{\Omega_0})^2 \Omega_{\text{SO}}^2, \quad (61)$$

From (61), it can be seen that

$$\frac{|\mathbf{G}_\mu(\mathbf{p}, s)|}{\Omega_{\text{SO}}} = \lambda^* + \frac{1}{\Omega_0}. \quad (62)$$

where $\lambda^* = 0$ due to (60). Therefore, when $|\mathbf{u}^*| = \Omega_{\text{SO}}$, the pointwise optimal control input satisfies

$$\mathbf{u}^*(\mathbf{p}) = (\mathbf{A}_\mu + \lambda^* \mathbf{I})^{-1} \mathbf{G}_\mu(\mathbf{p}, s) = \begin{bmatrix} \frac{G_{1\mu}(\mathbf{p}, s)}{\frac{1}{\Omega_0} + \lambda^*} \\ \frac{G_{2\mu}(\mathbf{p}, s)}{\frac{1}{\Omega_0} + \lambda^*} \end{bmatrix}. \quad (63)$$

where $\lambda^* = 0$ according to (60). Consequently, the equation in (63), when $|\mathbf{u}^*| = \Omega_{\text{SO}}$, is equivalent to

$$\mathbf{u}^*(\mathbf{p}, s) = \frac{\Omega_{\text{SO}}}{|\mathbf{G}_\mu(\mathbf{p}, s)|} \begin{bmatrix} G_{1\mu}(\mathbf{p}, s) \\ G_{2\mu}(\mathbf{p}, s) \end{bmatrix} = \frac{\Omega_{\text{SO}}}{|\mathbf{G}_\mu(\mathbf{p}, s)|} \mathbf{G}_\mu(\mathbf{p}, s). \quad (64)$$

Furthermore, if $|\mathbf{u}^*| < \Omega_{\text{SO}}$, then the pointwise optimal control input is given by $\mathbf{u}^*(\mathbf{p}, s) = -\mathbf{A}_\mu^{-1} \mathbf{G}_\mu(\mathbf{p}, s)$. Under $q_1 = q_2 = \frac{1}{\Omega_0 e_{11}^2}$, we have that $\mathbf{A}_\mu = e_{11}^2 q_1 \mathbf{I} = \frac{1}{\Omega_0} \mathbf{I}$. Therefore, if $|\mathbf{u}^*| < \Omega_{\text{SO}}$, then $\mathbf{u}^*(\mathbf{p}, s) = -\Omega_0 \mathbf{G}_\mu(\mathbf{p}, s)$. ■

One of the features of the ODS-based control solution to the microswimmer's LFC problem in (52) is that it is an absolutely continuous function of the position of the microswimmer. Indeed, the pointwise optimal control input in (52) is continuously differentiable for almost all values of the microswimmer's position \mathbf{p} and the dynamic variable s . Furthermore, it is a globally Lipschitz function of \mathbf{p} and s . The block diagram of our ODS-based control scheme is depicted in Figure 2(b) and our solution to the LFC problem is summarized as follows:

5 Simulation Results

In this section we present numerical simulation results to validate the performance of the ODS-based control

method described in Section 4.

Table 2 summarizes the parameters of the magnetic microswimmer used in our simulations, which are equal to the parameter values of the experimental helical swimmer prototype in [11]. The helical microrobot in [11], which *does not have* a magnetic head, swims in corn syrup with a viscosity of approximately $\eta_{\text{mod}} = 2500$ cps and a density of $\rho = 1.36$ g/ml. The mass of the magnetic swimmer is equal to 8.9 milligrams. The viscosity and density of the corn syrup along with the physical dimensions of the helical swimmer satisfy the low-Reynolds-number regime condition. We would like the microrobot to converge to $\mathcal{P} := \{p \in \mathbb{R}^2 : p = \tau \hat{e}_0, \tau \in \mathbb{R}\}$, where $\hat{e}_0 = [1, 0]^\top$, subject to control input saturation limit $\Omega_{\text{SO}} = 2.8$ Hz. In our simulation studies, we have assumed that knowledge of neither the weight of the microswimmer nor its environment are available. Hence, in all our simulations, we set $\hat{\mathbf{d}}_\mu = \mathbf{0}$ (lack of knowledge about the disturbances) and $\hat{e}_{11} = 1$ (lack of knowledge about the fluid environment and swimmer's physical parameters) in our control scheme. We have chosen the look-ahead distance parameter Δ_{LOS} in the ILOS guidance law in (27) to be equal to 0.75 mm. Furthermore, we have chosen $\alpha_d = 600$, $\sigma_0 = 0.01$, and $k_d = 0.15$. In the pointwise optimal control law in (52), we have chosen $\Omega_0 = 1$ Hz. In our simulation studies, we have initialized the microrobot position at $p(0) = [0 \text{ mm}, -40.0 \text{ mm}]^\top$. In addition to the proposed ODS-based scheme, where we use the ILOS-based guidance law, we also use an ODS-based scheme with the conventional LOS guidance law where there are no integral actions embedded in the guidance law in two different cases. In our first simulation study, we used the same parameters for the conventional LOS-based guidance law. In order to improve the tracking performance of the conventional LOS-based guidance law in the presence of unknown weight and microswimmer physical parameters, we increased the value of α_d in a second set of numerical simulations.

Plots in Figure 4 depict the path of the microrobot under the conventional and ILOS-based control inputs that have been generated using the ODS-based QP proposed in [15]. The inner-plots depict the time profile of the magnitude of the velocity vector of the microswimmer. Plots in Figure 5 depict the control input time profile under the conventional and ILOS-based control inputs that have been generated using the ODS-based QP. The mean value of the absolute of the cross-track error $|\varepsilon(t)|$ in the last 10 seconds of the simulation, i.e., when $90 \text{ sec} \leq t \leq 100 \text{ sec}$, were equal to 0.79 mm for the conventional LOS-based guidance law in [15] with $\alpha_d = 1200$, 1.8 mm for the conventional LOS-based guidance law in [15] with $\alpha_d = 600$, and 0.09 mm for the ILOS-based guidance law with $\alpha_d = 600$. Although, the tracking error performance of the conventional LOS-based guidance law gets improved with increasing the parameter α_d , the speed of rotation of the microswimmer remains very high throughout the simulations. In par-

Table 2

Symbol	Description	Numerical values in simulations
θ_h	Helix pitch angle.	45°
n_h	Number of turns of the helix.	3.5
r_h	Helix radius.	420 μm
$ \mathbf{d}_g $	Weight of the microswimmer.	8.7×10^{-5} N
e_{11}	Physical parameter of the microswimmer given by (8).	9.3×10^{-5} m

The physical parameters of the helical swimmer in [11].

particular, whereas the speed of rotation of the microswimmer with the ILOS-based guidance law is approximately equal to 0.17Hz during the steady state, the speed of rotation with the conventional guidance law remains higher (around 0.21Hz) during the steady state.

Discussion on the design parameters: There are four main parameters k_d , α_d , σ_0 , and Δ_{LOS} that appear in the ILOS-based control law in (27). As it can be seen from (30), the parameter α_d plays a direct role on the cross-track error dynamics. The role of the look-ahead distance parameter Δ_{LOS} and the parameter σ_0 is to simultaneously tune the rate of integration of s , which provides us with the integral action, with respect to the cross-track error and to provide a proper geometric direction for the microswimmer as manifested in (27). The parameter k_d adds a further damping action to the dynamic variable s in order to further improving its stability and preventing integrator wind-up. The inequality provided in (42) gives sufficient conditions for Proposition 4.3 to hold. As it can be seen from the chosen parameters in our simulation results $\frac{k_d}{\alpha_d} \geq 0$ and $(\sigma_0 \alpha_d \Delta_{\text{LOS}})^2 + 2\alpha_d \Delta_{\text{LOS}}(1 + \frac{k_d}{\alpha_d}) = 0.9$.

6 Concluding Remarks and Future Research Directions

Using the optimal decision strategy (ODS) framework and an integral-line-of-sight (ILOS) guidance law, we presented an optimization-based control solution for path following control of swimming helical magnetic microrobots subject to control input constraints. In addition to formally proving practical convergence to desired straight lines with absolutely continuous velocity profiles in the presence of disturbances, we also derived closed-form solutions for the pointwise optimal control input that results from the trust region subproblem (TRS) arising from the ODS framework for microrobot path following control. We can think of at least two limitations in our proposed ILOS-based control approach. The first limitation is due to the possibility of integrator wind-up, which is inherent to the ILOS-based family of controllers. Indeed, the role of the term $(\varepsilon + \sigma_0 s)^2$

in the ILOS-based control law is to decrease the risk of such phenomenon. The second limitation is due to the physics of the problem and the environment in which the microswimmer might be operating in. In particular, if the disturbances from the microswimmer's ambient environment have impulsive nature such as the systolic blood pressure, they might be able to violate the Hypotheses H1 (synchronous rotation with the external field) and H2 (alignment of the microswimmer central axis with the external field). Under this violation, a more complex dynamical model of the microswimmer such as the one provided in [42] would be needed for modifying our proposed ILOS-based control law.

The proposed methodology leads us to further research avenues for controlling helical magnetic microrobots such as way-point tracking control in the cluttered areas of the human body, three-dimensional maneuvering control, control in the presence of disturbances such as vessel blood flow, and control of a collection of microrobots moving in a formation.

References

- [1] F. Ullrich, C. Bergeles, J. Pokki, O. Ergeneman, S. Erni, G. Chatzipirpiridis, S. Pané, C. Framme, and B. J. Nelson, "Mobility experiments with microrobots for minimally invasive intraocular surgery," *Investig. Ophthalmol. Vis. Sci.*, vol. 54, no. 4, pp. 2853–2863, 2013.
- [2] K. Cha, S. Jeong, J. Choi, L. Qin, J. Li, J. Park, and S. Park, "Electromagnetic actuation methods for intravascular locomotive microrobot," in *Proc. Ann. Int. Conf. IEEE Eng. Med. Biol. Soc. (EMBC)*, Buenos Aires, Argentina, 2010, pp. 1962–1965.
- [3] H.-W. Tung, M. Maffioli, D. R. Frutiger, K. M. Sivaraman, S. Pané, and B. J. Nelson, "Polymer-based wireless resonant magnetic microrobots," *IEEE Trans. Robot.*, vol. 30, no. 1, pp. 26–32, 2013.
- [4] M. S. Sakar, E. B. Steager, D. H. Kim, M. J. Kim, G. J. Pappas, and V. Kumar, "Single cell manipulation using ferromagnetic composite microtransporters," *Appl. Phys. Lett.*, vol. 96, no. 4, p. 043705, 2010.
- [5] J. J. Abbott, K. E. Peyer, M. C. Lagomarsino, L. Zhang, L. Dong, I. K. Kaliakatsos, and B. J. Nelson, "How should microrobots swim?" *Int. J. Robot. Res.*, vol. 28, no. 11-12, pp. 1434–1447, 2009.
- [6] T. Honda, K. Arai, and K. Ishiyama, "Micro swimming mechanisms propelled by external magnetic fields," *IEEE Trans. Magn.*, vol. 32, no. 5, pp. 5085–5087, 1996.

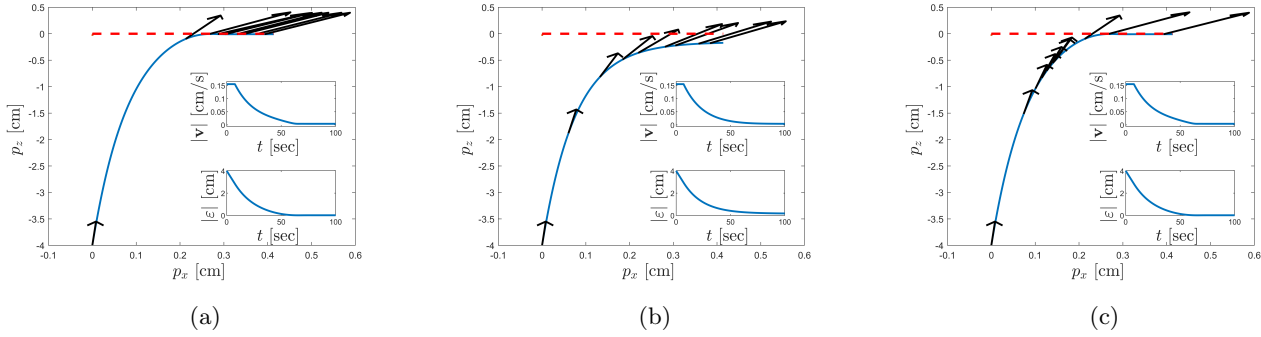


Fig. 4. Microrobot position along with cross-tracking error and magnitude of velocity: (a) the conventional ODS-based scheme in [15] with $\alpha_d = 1200$, (b) the conventional ODS-based scheme in [15] with $\alpha_d = 600$, and (c) the proposed ODS-based scheme with $\alpha_d = 600$.

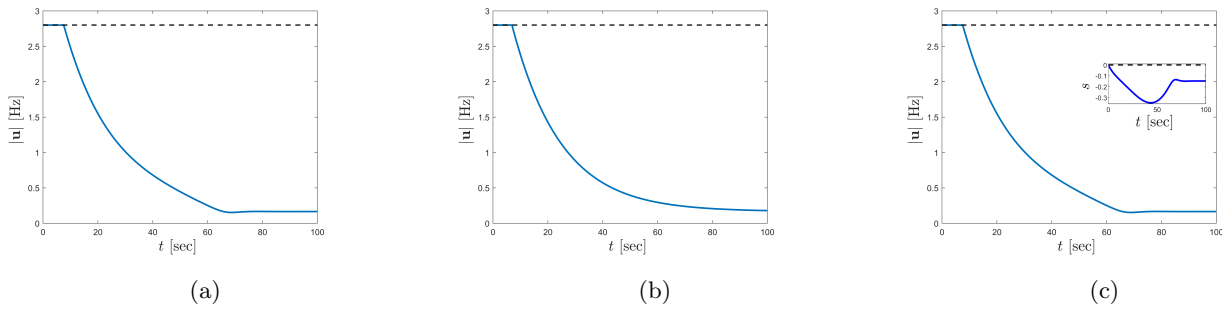


Fig. 5. Microrobot control input: (a) the conventional ODS-based scheme in [15] with $\alpha_d = 3000$, (b) the conventional ODS-based scheme in [15] with $\alpha_d = 600$, and (c) the proposed ODS-based scheme with $\alpha_d = 600$ and the adaptive variable s time profile.

- [7] B. Behkam and M. Sitti, "Design methodology for biomimetic propulsion of miniature swimming robots," *J. Dyn. Syst. Meas. Contr.*, vol. 128, no. 1, pp. 36–43, 2006.
- [8] K. B. Yesin, K. Vollmers, and B. J. Nelson, "Modeling and control of untethered biomicrobots in a fluidic environment using electromagnetic fields," *Int. J. Robot. Res.*, vol. 25, no. 5-6, pp. 527–536, 2006.
- [9] I. S. Khalil, A. F. Tabak, A. Hosney, A. Mohamed, A. Klingner, M. Ghoneima, and M. Sitti, "Sperm-shaped magnetic microrobots: Fabrication using electrospinning, modeling, and characterization," in *Proc. IEEE Int. Conf. Robot. Autom.*, Stockholm, Sweden, 2016, pp. 1939–1944.
- [10] D. J. Bell, S. Leutenegger, K. Hammar, L. Dong, and B. J. Nelson, "Flagella-like propulsion for microrobots using a nanocoil and a rotating electromagnetic field," in *Proc. IEEE Int. Conf. Robot. Automat.*, Rome, Italy, 2007, pp. 1128–1133.
- [11] A. W. Mahoney, J. C. Sarrazin, E. Bamberg, and J. J. Abbott, "Velocity control with gravity compensation for magnetic helical microswimmers," *Adv. Robot.*, vol. 25, no. 8, pp. 1007–1028, 2011.
- [12] H. Marino, C. Bergeles, and B. J. Nelson, "Robust electromagnetic control of microrobots under force and localization uncertainties," *IEEE Trans. Autom. Sci. Eng.*, vol. 11, no. 1, pp. 310–316, 2013.
- [13] L. Arcese, M. Fruchard, and A. Ferreira, "Adaptive controller and observer for a magnetic microrobot," *IEEE Trans. Robot.*, vol. 29, no. 4, pp. 1060–1067, 2013.
- [14] M. Fruchard, L. Arcese, and E. Courtial, "Estimation of the blood velocity for nanorobotics," *IEEE Trans. Robot.*, vol. 30, no. 1, pp. 93–102, 2013.
- [15] A. Mohammadi and M. W. Spong, "Path following control of swimming magnetic helical microrobots subject to step-out frequencies," in *Proc. IEEE Conf. Technol. Appl. (CCTA)*, Copenhagen, Denmark, 2018, pp. 60–66.
- [16] A. Pedram, H. N. Pishkenari, and M. Sitti, "Optimal controller design for 3d manipulation of buoyant magnetic microrobots via constrained linear quadratic regulation approach," *J. Micro-Bio Robot.*, vol. 15, no. 2, pp. 105–117, 2019.
- [17] B. Dahroug, J.-A. Seon, A. Oulmas, and T. Xu, "Some examples of path following in microrobotics," in *Int. Conf. Manip. Autom. Robot. Small Scales (MARSS)*, Nagoya, Japan, 2018, pp. 1–6.
- [18] A. P. Aguiar, J. P. Hespanha, and P. V. Kokotović, "Path-following for nonminimum phase systems removes performance limitations," *IEEE Trans. Automat. Contr.*, vol. 50, no. 2, pp. 234–239, 2005.
- [19] T. Xu, G. Hwang, N. Andreff, and S. Régnier, "Planar path following of 3-D steering scaled-up helical microswimmers," *IEEE Trans. Robot.*, vol. 31, no. 1, pp. 117–127, 2015.
- [20] A. Oulmas, N. Andreff, and S. Régnier, "Closed-loop 3D path following of scaled-up helical microswimmers," in *Proc. IEEE Int. Conf. Robot. Automat. (ICRA)*, Stockholm, Sweden, 2016, pp. 1725–1730.
- [21] X. Wu, J. Liu, C. Huang, M. Su, and T. Xu, "3-D path following of helical microswimmers with an adaptive orientation compensation model," *IEEE Trans. Autom. Sci. Eng.*, 2019.

- [22] A. Oulmas, N. Andreff, and S. Régnier, “3D closed-loop swimming at low Reynolds numbers,” *Int. J. Robot. Res.*, vol. 37, no. 11, pp. 1359–1375, 2018.
- [23] C. Samson, “Control of chained systems application to path following and time-varying point-stabilization of mobile robots,” *IEEE Trans. Autom. Contr.*, vol. 40, no. 1, pp. 64–77, 1995.
- [24] G. Kósa, M. Shoham, and M. Zaaroor, “Propulsion method for swimming microrobots,” *IEEE Trans. Robot.*, vol. 23, no. 1, pp. 137–150, 2007.
- [25] G. Cicconofri and A. DeSimone, “Motion planning and motility maps for flagellar microswimmers,” *The European Physical Journal E*, vol. 39, no. 7, p. 72, 2016.
- [26] B. Behkam and M. Sitti, “Modeling and testing of a biomimetic flagellar propulsion method for microscale biomedical swimming robots,” in *Proc. IEEE/ASME Adv. Intell. Mechatron. Conf.*, Monterey, CA, 2005, pp. 24–28.
- [27] T. W. Fountain, P. V. Kailat, and J. J. Abbott, “Wireless control of magnetic helical microrobots using a rotating-permanent-magnet manipulator,” in *Proc. IEEE Int. Conf. Robot. Autom. (ICRA)*, Anchorage, AK, 2010, pp. 576–581.
- [28] A. W. Mahoney, N. D. Nelson, K. E. Peyer, B. J. Nelson, and J. J. Abbott, “Behavior of rotating magnetic microrobots above the step-out frequency with application to control of multi-microrobot systems,” *Appl. Phys. Lett.*, vol. 104, no. 14, p. 144101, 2014.
- [29] B. J. Morris, M. J. Powell, and A. D. Ames, “Continuity and smoothness properties of nonlinear optimization-based feedback controllers,” in *Proc. IEEE Conf. Dec. Contr. (CDC)*, Osaka, Japan, 2015, pp. 151–158.
- [30] A. D. Ames, X. Xu, J. W. Grizzle, and P. Tabuada, “Control barrier function based quadratic programs for safety critical systems,” *IEEE Trans. Automat. Contr.*, vol. 62, no. 8, pp. 3861–3876, 2017.
- [31] K. Bouyarmane and A. Kheddar, “On weight-prioritized multitask control of humanoid robots,” *IEEE Trans. Automat. Contr.*, vol. 63, no. 6, pp. 1632–1647, 2017.
- [32] R. Thomas, J. Thorp, and C. Pottle, “A model-referenced controller for stabilizing large transient swings in power systems,” *IEEE Trans. Automat. Contr.*, vol. 21, no. 5, pp. 746–750, 1976.
- [33] M. W. Spong, J. S. Thorp, and J. M. Kleinwaks, “The control of robot manipulators with bounded input: Part II: Robustness and disturbance rejection,” in *Proc. IEEE Conf. Dec. Contr. (CDC)*, vol. 23, Las Vegas, NV, 1984, pp. 1047–1052.
- [34] M. Spong, J. Thorp, and J. Kleinwaks, “The control of robot manipulators with bounded input,” *IEEE Trans. Automat. Contr.*, vol. 31, no. 6, pp. 483–490, 1986.
- [35] T. I. Fossen, K. Y. Pettersen, and R. Galeazzi, “Line-of-sight path following for dubins paths with adaptive sideslip compensation of drift forces,” *IEEE Trans. Contr. Syst. Technol.*, vol. 23, no. 2, pp. 820–827, 2014.
- [36] W. Caharija, K. Y. Pettersen, M. Bibuli, P. Calado, E. Zereik, J. Braga, J. T. Gravdahl, A. J. Sørensen, M. Milovanović, and G. Bruzzone, “Integral line-of-sight guidance and control of underactuated marine vehicles: Theory, simulations, and experiments,” *IEEE Trans. Contr. Syst. Technol.*, vol. 24, no. 5, pp. 1623–1642, 2016.
- [37] S. Adachi, S. Iwata, Y. Nakatsukasa, and A. Takeda, “Solving the trust-region subproblem by a generalized eigenvalue problem,” *SIAM J. Optim.*, vol. 27, no. 1, pp. 269–291, 2017.
- [38] W. W. Hager, “Minimizing a quadratic over a sphere,” *SIAM J. Optim.*, vol. 12, no. 1, pp. 188–208, 2001.
- [39] G. E. Forsythe and G. H. Golub, “On the stationary values of a second-degree polynomial on the unit sphere,” *J. Soc. Ind. Appl. Math.*, vol. 13, no. 4, pp. 1050–1068, 1965.
- [40] W. Caharija, M. Candeloro, K. Y. Pettersen, and A. J. Sørensen, “Relative velocity control and integral los for path following of underactuated surface vessels,” *IFAC Proceedings Volumes*, vol. 45, no. 27, pp. 380–385, 2012.
- [41] H. K. Khalil, *Nonlinear Systems*, 3rd ed. Upper Saddle River, NJ: Prentice Hall, 2002.
- [42] A. W. Mahoney, N. D. Nelson, E. M. Parsons, and J. J. Abbott, “Non-ideal behaviors of magnetically driven screws in soft tissue,” in *2012 IEEE/RSJ Int. Conf. Intell. Robot. Syst.*, 2012, pp. 3559–3564.